DIRECTED MIGRATION OF MICROSCALE SWIMMERS BY AN ARRAY OF SHAPED OBSTACLES: MODELING AND SHAPE OPTIMIZATION*

JIAJUN TONG† AND MICHAEL J. SHELLEY†‡

Abstract. Achieving macroscopic directed migration of microscale swimmers in a fluid is an important step towards utilizing their autonomous motion. It has been experimentally shown that directed motion can be induced, without any external fields, by certain geometrically asymmetric obstacles due to interaction between their boundaries and the swimmers. In this paper, we propose a kinetic-type model to study swimming and directional migration of microscale bimetallic rods in a periodic array of posts with noncircular cross-sections. Both rod position and orientation are taken into account; rod trapping and release on the post boundaries are modeled by empirically characterizing curvature and orientational dependence of the boundary absorption and desorption. Intensity of the directed rod migration, which we call the normalized net flux, is then defined and computed given the geometry of the post array. We numerically study the effect of post spacings on the flux; we also apply shape optimization to find better post shapes that can induce stronger flux. Inspired by preliminary numerical results on two candidate posts, we perform an approximate analysis on a simplified model to show the key geometric features that a good post should have. Based on this, three new candidate shapes are proposed which give rise to large fluxes. This approach provides an effective tool and guidance for experimentally designing new devices that induce strong directed migration of microscale swimmers.

1. Introduction. Microscale swimmers, such as bacteria or chemically active colloids, move autonomously in a fluid by converting energy in the local environment into mechanical work [10, 9]. Possible applications of synthetic microswimmers include drug delivery [25, 2], cargo transport [32], and environmental remediation [30]. One important task in manipulating microswimmers is to achieve their directed macroscopic motion, as opposed to their long-time isotropic motion, which results from a combination of ballistic swimming and angular diffusion [13, 24]. Directed migration can be easily induced by externally imposed fields, such as chemical gradient [3, 21] or electromagnetic fields [1, 12, 36, 34]. A different approach is to place obstacles in the environment. It has been demonstrated that obstacles can dramatically change the motion of microswimmers. Due to hydrodynamic or steric interactions [31, 6, 14, 20] of swimmers with obstacles, swimmers can aggregate [17, 18, 4], slide [36, 31, 33], hover [35], or even reverse swimming direction [5]. There is a developing body of works investigating boundaries of obstacles guiding microswimmers, using flat walls [36], v-shaped funnels [11, 16], spherical obstacles [31, 33, 28], or teardrop-shaped posts [40].

In a series of recent works, microscale bimetallic segmented rods composed of gold

†Applied Mathematics Lab, Courant Institute, New York University, New York, NY 10012 (jiajun@cims.nyu.edu, shelley@cims.nyu.edu).
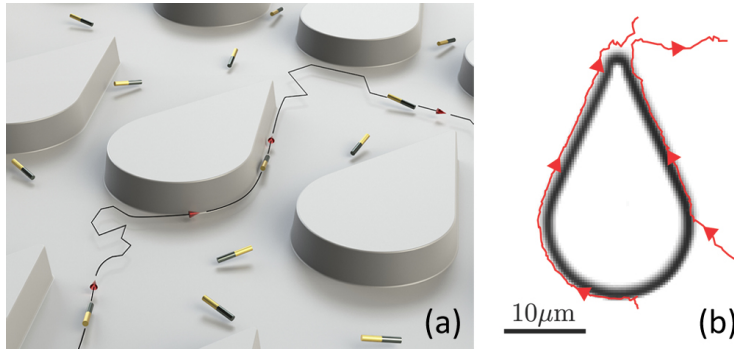‡Flatiron Institute, Simons Foundation, New York, NY 10010.

FIG. 1. (a) *Sketch of bimetallic microscale Au-Pt rods swimming and interacting with an array of teardrop-shaped posts. These rods swim, due to self-electrophoresis, primarily along the bottom of the posts. They move along their axes with the Pt-end leading; their positions and orientations are subject to random fluctuations. After encountering a post, swimming rods tend to travel along the post boundary and preferentially depart from its tip.* (b) *Experimental observation of two typical trajectories of swimming rods when interacting with a teardrop-shaped post. The pictures are adapted from our recent experimental paper* [40].

and platinum (Au-Pt) have been experimentally studied as a prototype of artificial microswimmers [33, 26]. These rods, typically $2\,\mu$m in length and 300 nm in diameter, move autonomously in aqueous solutions of hydrogen peroxide (H_2O_2), with the Pt end leading, due to self-electrophoresis which generates a slip flow along the rod surface [23, 38]. They move with a constant speed along their axes while their positions and orientations are subject to random fluctuations. As they are much denser than water, the Au-Pt rods swim primarily along the microscope coverslip or the obstacles. It is demonstrated in our paper [33] that these swimming rods can be captured by solid spheres resting on a horizontal plane, and orbit closely around them with little change in their speed, until they are released due to angular diffusion. An uneven spatial distribution of the rods near the spheres and statistics of trapping time are obtained. In a more recent study [40], we show that when the rods swim in a periodic array of teardrop-shaped posts, they interact with the vertical walls of the posts in a similar way; yet the rods preferentially leave the posts at the post's sharp tips due to large boundary curvature there, rendering a statistically biased swimming over long times. See Figure 1 for a sketch of the rods swimming and interacting with an array of teardrop-shaped posts, as well as a picture from the experiment showing typical motion of rods when they encounter a post [40]. It has been experimentally confirmed that the rods are most likely to migrate through the array in the direction pointed by the tips of the teardrop-shaped posts [40].

In this paper, we shall present a kinetic-type model of Au-Pt rods swimming in a periodic array of posts with noncircular cross-sections, such as teardrop-shaped posts, and thus generating directed migration over a long time. Position and orientation of the rods are both taken into account, as well as the effect of thermal fluctuation. Trapping and release of the rods on the post boundary are modeled via empirically defined rate functions and angular distributions, accounting for curvature and orientational dependence of the boundary absorption and desorption, respectively. Distributions of the rods in the free space and on the post boundary are found through numerical simulations; the intensity of the directed migration is then defined and calculated.

The degree of directed migration crucially relies on many features of the array,

such as the spacings and shapes of the posts in it. We study the effect of post spacing by numerical simulation. We also perform numerical shape optimization to investigate how to choose the shape of posts judiciously so that stronger directed migration of the swimming rods is achieved. General theory of shape optimization is well established from an analysis point of view [29, 7, 27], while numerous applications can be found in many areas of applied mathematics and physics, such as problems involving swimming [15, 39] and fluid motion [37, 22]. In our study, a mathematical derivation of the shape optimization is presented in the supplementary material, together with an iterative optimization method based on an explicitly preconditioned steepest ascent method. We apply shape optimization to two candidate post shapes and observe a significant increase in directed migration. To better understand the optimization results, we propose a simplified model that well explains the geometric features arising in the optimized shape. This enables us to empirically determine the key geometric ingredients of designing posts. We conclude by giving three new post shapes designed on these ingredients, which does give rise to a significantly stronger directed migration than naive choices.

The rest of the paper is organized as follows. In subsection 2.1, we present the model for Au-Pt rods swimming in a periodic rectangular array of posts and define the quantity that measures the intensity of the directed migration. The numerical method to compute the ensemble distributions of rod positions and orientations as well as the intensity of the directed migration appear in the supplementary material. In subsection 2.2, we formulate the optimization problem seeking better designs of the array so that it induces stronger directed migration. A formal overview of the shape optimization theory, a full derivation of equations involved, and numerical methods for solving these equations and performing shape optimization are also left to the supplementary material. Dimensionless parameters and rates are specified in section 3, while numerical results are presented in section 4 to study the effects of post spacings and optimization of post shape. To understand the key geometric features that a good post should have, we perform an approximate analysis to a simplified model in section 5. Based on that, three new post designs inducing strong directed migration are proposed in section 6. We conclude the paper with a brief discussion in section 7.

2. Theory.

2.1. Modeling microscale swimming rods in a periodic array of posts. With the typical swimming pattern of the rod described in section 1 and sketched in Figure 1, we shall build a kinetic-type model for rods swimming in a periodic array of posts. The model will be presented in a dimensionless manner; the nondimensionalization will be left to section 3. We start by modeling the environment in which the rods are swimming.

Consider a rectangular periodic array of posts printed on the microscope coverslip. The posts are solid cylinders which neither fluid nor the rods can penetrate [40]. A dilute suspension of the Au-Pt rods in the aqueous hydrogen peroxide solution is then placed on the coverslip, so that the rods can autonomously swim in the complex landscape. Note that since the rods always swim in a quasi-two-dimensional fashion along the bottom, it suffices to consider the system in two dimensions. Assume the two-dimensional unit cell of the periodic array of the posts has dimensionless size a and b in x_1- and x_2-directions, respectively. We denote the unit cell to be $Y = \left[-\frac{a}{2}, \frac{a}{2}\right] \times \left[-\frac{b}{2}, \frac{b}{2}\right]$. See Figure 2. The following discussion also applies to unit cells in other shapes with minor modification. For example, for a staggered periodic array, hexagonal unit cells can be more convenient choices than rectangular ones.
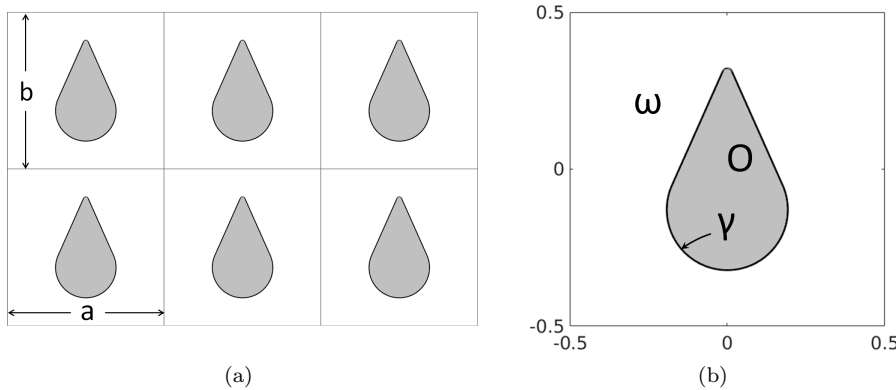
FIG. 2. (a) *A periodic array of teardrop-shaped posts. Its unit cells, separated by solid lines, have width a and height b; here a = b = 1. Domains occupied by the posts are depicted as gray.* (b) *An enlarged view of one unit cell in* (a). *O denotes the gray domain occupied by the post; ω denotes the exterior domain filled with fluid; γ denotes the boundary of ω between them.*

In what follows, for convenience we will interchangeably use the notion of a post and its cross-section. Let O denote the domain occupied by the post inside Y, and let $\omega = Y \backslash O$ be the domain filled with fluid, in which the rods can swim freely. The interior and exterior boundaries of ω are denoted by $\gamma = \partial O$ and ∂Y, respectively; see Figure 2(b).

To study the statistical behavior of the swimming rods, we look at the spatial and orientational distribution of an ensemble of rods in the bulk and on the boundary. We assume that the rod concentration is so small that their interactions are negligible. We also treat the rods as points with orientation but no size.

The motion of the rods is modeled as swimming in the bulk ω and swimming along the boundary γ. For a single rod swimming in the bulk, we use $X_t \in \omega$ and $2\pi\Theta_t$ to denote its position and orientation, respectively. The latter is the angle between the swimming direction of the rod and the positive x_1-axis; see Figure 3. Here X_t is defined up to a natural periodicity on the exterior boundary of ω, while $\Theta_t \in [0, 1)$ defined in the modulus of 1. We assume that the rod deterministically swims in its axial direction with velocity v_0, while both its position and orientation are subject to random fluctuations. The stochastic dynamics of (X_t, Θ_t) is then written as follows:

(2.1)
$$dX_t = v_0(\cos(2\pi\Theta_t), \sin(2\pi\Theta_t))^T + \sqrt{2D_t}dW_t^{(2)},$$
$$d\Theta_t = \sqrt{2D_r}dW_t^{(1)}.$$

Here D_t and D_r are scalar (dimensionless) translational and rotational diffusion coefficients, respectively; they are assumed to be constant throughout the state space $\Omega \triangleq \omega \times [0, 1]$. $W_t^{(1)}$ and $W_t^{(2)}$ are the standard Brownian motions in one and two dimensions, respectively; they are independent of each other. Let $p(x, \theta, t) \geq 0$ be the distribution of rods in Ω, where $x \in \omega$ and $2\pi\theta \in [0, 2\pi]$. The evolution of p is then governed by the following Fokker–Planck equation associated with (2.1):
(2.2)
$$\partial_t p(x, \theta, t) = D_t \Delta_x p(x, \theta, t) + D_r \Delta_\theta p(x, \theta, t) - v_0(\cos 2\pi\theta, \sin 2\pi\theta)^T \cdot \nabla_x p(x, \theta, t).$$

Here $(x, \theta) \in \Omega$; $\Delta_x = \partial_{x_1 x_1} + \partial_{x_2 x_2}$, and $\Delta_\theta = \partial_{\theta\theta}$; $\nabla_x = (\partial_{x_1}, \partial_{x_2})^T$ is the gradient operator in spatial components only. The term $-v_0(\cos 2\pi\theta, \sin 2\pi\theta)^T \cdot \nabla_x p$ represents
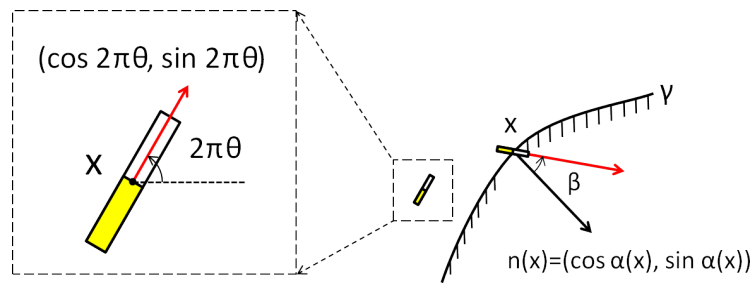
FIG. 3. *We use $x \in \omega$ and $2\pi\theta$, with $\theta \in [0,1)$, to represent position and orientational angle of a swimming Au-Pt rod, respectively. The enlarged picture in the big dashed box shows the state (x,θ) of the rod in the small dashed box, which is swimming away from the post. The red arrow represents its orientation, given by the direction of its Pt end (white block); the dashed line is the positive x_1-axis. Note that rods are modeled as points with orientation but no size, although we have drawn a white-yellow rod in the picture for the sake of clarity. In the right half of the figure, with abuse of notation, a rod hitting the post boundary γ at x with relative angle β is shown. The shaded side of γ is occupied by the post. The black arrow is the normal vector of γ at x, denoted by $n(x) = (\cos\alpha(x), \sin\alpha(x))$, while the red arrow again represents the rod orientation. The (signed) angle between them is the relative angle β. (Color available online.)*

convection in Ω due to the directed swimming in the axial direction.

For rods moving along the boundary γ, we assume they always swim tangentially to γ; thus only the rod position along γ needs to be considered. We also assume that rods swim at the constant speed v_0 [33] and can never switch swimming direction before leaving the boundary. This assumption is suitable for bimetallic swimming rods, but might not be true for some biological swimmers [5]. For $x \in \gamma$, let $p_B^+(x,t), p_B^-(x,t) \geq 0$ be the boundary distributions of rods that swim counterclockwise and clockwise, respectively. The evolution of $p_B^\pm$'s is given by

$$(2.3) \qquad \partial_t p_B^\pm(x,t) = D_t \Delta_\gamma p_B^\pm(x,t) \mp v_0 \partial_\gamma p_B^\pm(x,t) + F_{\text{in}}^\pm(x,t) - F_{\text{out}}^\pm(x,t), \quad x \in \gamma,$$

where Δ_γ and ∂_γ are the Laplace operator and the derivative along γ with respect to its arclength. Here γ is parameterized counterclockwise. On the right-hand side of (2.3), $D_t \Delta_\gamma p_B^\pm$ is the spatial diffusion along γ; for simplicity, we assume the same diffusion coefficient D_t as in the free space. The term $\mp v_0 \partial_\gamma p_B^\pm(x,t)$ comes from the deterministic swimming along γ. $F_{\text{in}}^\pm(x,t)$ and $F_{\text{out}}^\pm(x,t)$ are rod absorption and desorption fluxes at x on and off the boundary γ, respectively. They depend on the local geometry of γ and how rods hit or leave the boundary.

To model this pair of fluxes, we need some notation. Let $\kappa(x)$ be the curvature of γ at x, and let $\alpha(x)$ be the orientation of the outer normal of γ at x with respect to ω; i.e., the normal vector is given by $(\cos\alpha(x), \sin\alpha(x))^T$. When a rod appears at a boundary point $x \in \gamma$ with orientational angle $2\pi\theta$, we define its relative angle with respect to γ to be $\beta = 2\pi\theta - \alpha(x) \pmod{2\pi}$; see Figure 3. To this end, we introduce empirical rate functions $r_{\text{in}}(\kappa)$ and $r_{\text{in}}(\kappa)$, and angular functions $\rho_\pm(\beta)$ and $\tau_\pm(\beta)$, to be explained later, and write

$$(2.4) \qquad F_{\text{in}}^\pm(x,t) = r_{\text{in}}(\kappa(x)) \int_0^1 p(x,\theta,t)\rho_\pm(2\pi\theta - \alpha(x))\, d\theta, \quad x \in \gamma,$$

$$(2.5) \qquad F_{\text{out}}^\pm(x,t) = r_{\text{out}}(\kappa(x)) p_B^\pm(x,t) \int_0^1 2\pi\tau_\pm(2\pi\theta - \alpha(x))\, d\theta, \quad x \in \gamma.$$

Here $r_{\text{in}}(\kappa)$ and $r_{\text{out}}(\kappa)$ are called absorption and desorption (Poisson) rates, respec-
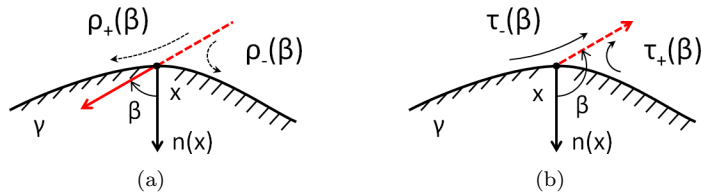
FIG. 4. $\rho_\pm(\beta)$ and $\tau_\pm(\beta)$. The black curve represents γ, and the shaded side is occupied by the post. The black arrow is the normal vector $n(x)$ of γ at x, while the red arrow represents the direction in which the rod hits γ, or the potential direction in which the rod is going to leave γ. (a) When the rod hits γ with relative angle β, it will have probabilities $\rho_+(\beta)$ and $\rho_-(\beta)$, respectively, of swimming counterclockwise and clockwise afterwards along γ. (b) When a rod is going to leave γ, its relative angle β with respect to γ is determined via the distributions $\tau_\pm(\beta)$. The subscripts indicate its original swimming direction before leaving γ. (Color available online.)

tively, which are assumed to be functions of curvature only. In fact, experiments have shown that at least the desorption rate also depends on the rod speed [40]. However, our assumption is valid since the rod speed is fixed to be v_0. The functions $r_{in}(\kappa(x))$ and $r_{out}(\kappa(x))$ then characterize how fast the boundary γ can absorb and desorb rods at $x \in \gamma$, respectively. Their precise characterization will be clear after we choose the characteristic scales and do nondimensionalization in section 3. The functions $\rho_\pm(\beta)$ account for the orientation dependence in the absorption. We assume that rods hitting γ with relative angle β will have probabilities $\rho_+(\beta)$ and $\rho_-(\beta)$ of subsequently swimming counterclockwise and clockwise along γ, respectively; see Figure 4(a). To make sense of (2.4), we note that rods hitting $x \in \gamma$ can come from the bulk in all directions; the function $r_{in}(\kappa(x))p(x,\theta,t)\rho_+(2\pi\theta - \alpha(x))$ is the amount of rods getting absorbed at x with angle $2\pi\theta$, and sliding counterclockwise along γ afterwards. The function $r_{in}(\kappa(x))p(x,\theta,t)\rho_-(2\pi\theta - \alpha(x))$ can be interpreted similarly. If we take an integral over all possible orientations of the incoming rods, we obtain the absorption fluxes.

Similarly, for desorption, rods that are leaving γ are assumed to leave at a random angle, with its probability distribution characterized by $\tau_\pm(\beta)$, where β is the relative angle defined before. The subscripts $\pm$ indicate the rods originally move counterclockwise or clockwise before leaving γ; see Figure 4(b). We argue as before to obtain (2.5). Via β and the tangent direction of γ, the initial orientational angle of the rod when it returns to the bulk can be determined. This will be useful in deriving the boundary condition of p below.

To summarize, the assumptions on r_{in}, r_{out}, $\rho_\pm$, and $\tau_\pm$ are as follows:
1. $r_{in}(\kappa)$, $r_{out}(\kappa) \geq 0$;
2. $\rho_\pm(\beta) \geq 0$ and $\rho_+(\beta) + \rho_-(\beta) \leq 1$;
3. $\tau_\pm(\beta) \geq 0$ and $\int_{-\pi}^{\pi} \tau_\pm(\beta)\,d\beta = 1$;
4. $\rho_+(\beta) = \rho_-(-\beta)$ and $\tau_+(\beta) = \tau_-(-\beta)$, by symmetry.

Since $\tau_\pm$'s are normalized, (2.5) reduces to $F_{out}^\pm = r_{out}p_B^\pm$.

Last, the boundary condition of p on $\Gamma \triangleq \gamma \times [0,1]$, the inner curved part of $\partial\Omega$, is derived from the conservation law, which gives

$$
(2.6) \quad \begin{aligned}
&D_t \frac{\partial p}{\partial n_\Gamma}(x,\theta,t) - v_0 p(x,\theta,t) \cdot (\cos 2\pi\theta, \sin 2\pi\theta, 0) \cdot n_\Gamma(x) \\
&= r_{out}(\kappa(x))[p_B^+(x,t) \cdot 2\pi\tau_+(2\pi\theta - \alpha(x)) + p_B^-(x,t) \cdot 2\pi\tau_-(2\pi\theta - \alpha(x))] \\
&\quad - r_{in}(\kappa(x))p(x,\theta,t)[\rho_+(2\pi\theta - \alpha(x)) + \rho_-(2\pi\theta - \alpha(x))].
\end{aligned}
$$

Here $(x, \theta) \in \Gamma$, and $n_\Gamma(x) = (\cos \alpha(x), \sin \alpha(x), 0)^T$ is the unit outer normal vector of Γ with respect to Ω. The left-hand side of (2.6) represents the boundary flux at $(x, \theta) \in \Gamma$ generated by the spatial diffusion and the swimming; it is balanced by the flux coming into the bulk due to desorption and absorption on the right-hand side. Using the formula for n_Γ, (2.6) is simplified to be

$$D_t \frac{\partial p}{\partial n_\Gamma}(x, \theta, t) - v_0 p(x, \theta, t) \cos \beta = 2\pi r_{\text{out}}(\kappa(x))[p_B^+(x, t)\tau_+(\beta) + p_B^-(x, t)\tau_-(\beta)]$$
$$- r_{\text{in}}(\kappa(x))p(x, \theta, t)[\rho_+(\beta) + \rho_-(\beta)],$$

with $\beta = 2\pi\theta - \alpha(x)$. For the outer flat surfaces of $\partial\Omega$, i.e., $\partial\Omega\backslash\Gamma$, we assign periodic boundary conditions for p.

In this paper, we shall only consider the steady-state solution. Indeed, thanks to the diffusions in the model, the initial distribution will converge to the steady-state solution after a relatively short transient stage; see section 3 for further discussion on the time scale. We omit the t-dependence in (2.2) and (2.3), and the equations become

(2.7)

$$D_t \Delta_x p(x, \theta) + D_r \Delta_\theta p(x, \theta) - v_0 (\cos 2\pi\theta, \sin 2\pi\theta)^T \cdot \nabla_x p(x, \theta) = 0, \quad (x, \theta) \in \Omega,$$

(2.8)

$$- D_t \Delta_\gamma p_B^\pm(x) \pm v_0 \partial_\gamma p_B^\pm(x) = \int_0^1 f_\pm(x, \theta) \, d\theta, \quad x \in \gamma,$$

(2.9)

$$D_t \frac{\partial p}{\partial n_\Gamma}(x, \theta) - v_0 p(x, \theta) \cos \beta + f_+(x, \theta) + f_-(x, \theta) = 0, \quad (x, \theta) \in \Gamma,$$

(2.10)

p satisfies periodic boundary condition on $\partial\Omega\backslash\Gamma$,

where $\beta = 2\pi\theta - \alpha(x)$ and

(2.11) $\qquad f_\pm(x, \theta) = r_{\text{in}}(x)\rho_\pm(\beta)p(x, \theta) - r_{\text{out}}(x) \cdot 2\pi\tau_\pm(\beta)p_B^\pm(x), \quad (x, \theta) \in \Gamma.$

Since we are describing the probability distribution of rods, the following normalization condition is needed:

(2.12) $\qquad N(\Omega) \triangleq \int_\Omega p(x, \theta) \, dxd\theta + \int_\gamma [p_B^+(x) + p_B^-(x)] \, d\gamma = 1.$

Note that if (2.12) is not assumed, then (p, p_B^+, p_B^-) being a solution of (2.7)–(2.11) implies that $(\lambda p, \lambda p_B^+, \lambda p_B^-)$ is also a solution $\forall \lambda > 0$.

Suppose we have obtained a nontrivial solution (p, p_B^+, p_B^-) to (2.7)–(2.11) (obviously $(0, 0, 0)$ is a trivial solution which is not interesting), without necessarily satisfying (2.12). We wish to characterize the intensity of the spontaneous directed migration of the rods induced by the post in some particular direction, say the positive x_2-direction. In our model, it is exactly the probability flux crossing the part of $\partial\Omega$ where $x_2 = b/2$. The unnormalized net flux is defined to be

(2.13) $\qquad F(\Omega) = \int_{\partial\Omega \cap \{x_2=b/2\}} -D_t \frac{\partial p}{\partial x_2} + v_0 p \sin 2\pi\theta \, dA.$

The first term comes from the spatial diffusion of rods, while the second is due to the directed swimming, where the rod orientation plays a role. Since this flux is generated by an amount of rods given by $N(\Omega)$, the normalized net flux is thus defined to be $E(\Omega) \triangleq F(\Omega)/N(\Omega)$. $E(\Omega)$ will be the key quantity in the rest of the paper.

The numerical method for solving the coupled system (2.7)–(2.11) and computing $E(\Omega)$ will be given in the supplementary material.

2.2. Seeking stronger directed migration of the rods. It is clear that the intensity of the directed migration of the rods is governed by many geometric features of the array, such as the sizes of gaps between neighboring posts, and the shapes of posts. An interesting and practical question to ask is how one might make the directed migration stronger by cleverly designing the array and post shapes. In our model, this could be formulated as the following optimization problem: given the functions $r_{\mathrm{in}}(\kappa)$, $r_{\mathrm{out}}(\kappa)$, $\rho_{\pm}(\beta)$, and $\tau_{\pm}(\beta)$, find $Y = \left[-\frac{a}{2}, \frac{a}{2}\right] \times \left[-\frac{b}{2}, \frac{b}{2}\right]$ and $\omega \subset Y$, such that $E(\Omega)$ is maximized.

This is an infinite-dimensional optimization problem, and finding the actual maximizer would be very hard. We are only able to pose it formally. Our strategy here is as follows. First, we shall study how the spacings of the posts affect $E(\Omega)$, simply by fixing the shape of the post and tuning a and b to see how $E(\Omega)$ changes. Second, we would like to look for a better post shape. Using the theory of shape optimization, we develop a numerical method that evolves γ in an iterative manner, so that the corresponding $E(\Omega)$ keeps increasing with each iteration. The mathematical formulation of the shape optimization problem is exceedingly long. We shall leave an overview of the theory of shape optimization, a complete derivation of the equations for the shape optimization, and an introduction of the associated numerical method to the supplementary material.

3. Model choices. Before presenting numerical results, we specify the dimensionless parameters and rates used in the simulations.

We take the characteristic length scale in the model to be the typical size of the unit cell in the experiment [40], which is $L = 45\,\mu\mathrm{m}$. We use the angular diffusion of the rods to determine the characteristic time scale. In the experiments, the typical angular diffusion scale is 0.5 rad/s. Hence, we take the characteristic time scale to be $T = 4\pi$ s. In this way, the dimensionless angular diffusion coefficient is $D_r = 1$; note that it is $2\pi\theta$ instead of θ that represents the rod orientation.

With the above choice, we take the dimensionless parameter in the model as follows: $D_t = 0.002$, $D_r = 1$, and $v_0 = 1$. Indeed, this corresponds to the case where the spatial diffusion of rods is approximately $0.002 \cdot [45\,\mu\mathrm{m}]^2/[4\pi\,\mathrm{s}] \approx 0.322\,\mu\mathrm{m}^2/\mathrm{s}$; the angular diffusion is 0.5 rad/s; and rods swim with approximate speed $1 \cdot [45\,\mu\mathrm{m}]/[4\pi\,\mathrm{s}] \approx 3.58\,\mu\mathrm{m}/\mathrm{s}$. All of these agree qualitatively with the measurements in the typical experiments [40]. It is also worthwhile to remark that the experiments usually last 10–20 minutes, which is significantly longer than the characteristic time scale T. This implies that even if the initial rod distribution is not the steady-state solution, the transient stage would be relatively short; after that, the system is well characterized by the stationary model.

There exists little systematic measurement of $r_{\mathrm{in}}(\kappa)$, $r_{\mathrm{out}}(\kappa)$, $\rho_{\pm}(\beta)$, and $\tau_{\pm}(\beta)$. We shall take them to be functions that qualitatively agree with the existing experimental observations or physical intuition.

We take $r_{\mathrm{in}}(\kappa) = 1$, which implies that the efficacy of the post boundary absorbing rods does not depend on the curvature. More precisely, given the unit density of rods (one rod per unit cell, i.e., $\frac{1}{45^2}\,\mathrm{rod}/\mu\mathrm{m}^2$) in the vicinity of the post boundary, there

is on average one absorbing event occurring over a boundary section with arclength $45\,\mu m$ every $4\pi\,s \approx 12.6\,s$, which is on the right scale.

The function $r_{\text{out}}(\kappa)$ is experimentally defined as the inverse of the expected trapping time of rods sliding along a circular boundary with the constant dimensionless curvature κ. Existing experiments indicate that for swimming Au-Pt rods [40] or swimming Janus particles [28], $r_{\text{out}}(\kappa)$ is an increasing function of κ. In other words, the efficacy of the boundary releasing rods should be higher where its curvature is larger (more convex). We take

$$(3.1) \qquad r_{\text{out}}(\kappa) = \frac{10}{\pi} \arctan\left(\frac{\kappa - 20}{4}\right) + 5$$

as a convenient choice; see Figure 5(a). Note that here $r_{\text{out}}(\kappa)$ saturates as $\kappa \to +\infty$; it is not a necessary feature but it can make the simulations more tractable. We shall also discuss this in subsection 4.2. To give a sense of the choice of $r_{\text{out}}(\kappa)$, we have $r_{\text{out}}(20) = 5$, which implies that when a rod is sliding along the boundary of a circular post with radius $2.25\,\mu m = [45\,\mu m]/20$, the expected sliding time is $\frac{4\pi}{5}\,s \approx 2.51\,s$. In other words, the Poisson rate of a rod leaving a circular boundary with radius $2.25\,\mu m$ is about $0.398\,s^{-1}$, which agrees qualitatively with the experimental data [40].

As a convenient choice, $\rho_\pm(\beta)$ are taken to be

$$(3.2) \qquad \rho_\pm(\beta) = \mp\frac{1}{\pi}\beta + \frac{1}{2}, \quad \beta \in [-\pi/2, \pi/2],$$

and $\rho_\pm(\beta) \equiv 0$ for $\beta \in [-\pi, \pi/2] \cup (\pi/2, \pi)$, which are plotted in Figures 5(b) and 5(c). This implies that when a rod hits the boundary perpendicularly ($\beta = 0$), it has equal probability of going in either direction along the boundary. When it approaches in the tangent directions ($\beta = \pm\pi/2$), it will go forward in the very direction with probability 1. When a rod reaches the boundary with its orientation pointing away from the boundary ($\beta \in [-\pi, \pi/2] \cup (\pi/2, \pi)$), it will not get absorbed. Indeed, the last case can arise when spatial diffusion pushes the rod to the boundary even though its orientation points away.

In our earlier study [33], a model based on lubrication theory indicates that the swimming rods are unlikely to leave the surface with small takeoff angles (i.e., the unsigned angle between the boundary and the rods)—in such a case, the rod tends to be pushed back towards the wall instead of detaching. A threshold value of $\pi/9$ of the takeoff angle is also taken in a subsequent stochastic simulation to fit the experimental distribution of the trapping times. To incorporate these facts, we take

$$(3.3) \qquad \tau_+(\beta) = \begin{cases} \frac{3}{2}\cos(3\beta) & \text{for } \beta \in [-5\pi/6, -\pi/2], \\ 0 & \text{for } \beta \in [-\pi, -5\pi/6) \cup (-\pi/2, \pi), \end{cases}$$

and $\tau_-(\beta) = \tau_+(-\beta)$, which are plotted in Figures 5(d) and 5(e), respectively. In this setting, rods can detach with the takeoff angle ranging from 0 to $\pi/3$ ($\beta \in [-5\pi/6, -\pi/2]$ for rods originally sliding counterclockwise on γ, or $\beta \in [\pi/2, 5\pi/6]$ for rods sliding clockwise). The most likely takeoff angle is $\pi/6$ ($\beta = -2\pi/3$ for rods sliding counterclockwise, or $\beta = 2\pi/3$ for rods sliding clockwise).

4. Numerical results. With implementation details now behind us, in this section, we shall present numerical results concerning how post spacings and post shapes can affect the normalized net flux $E(\Omega)$.
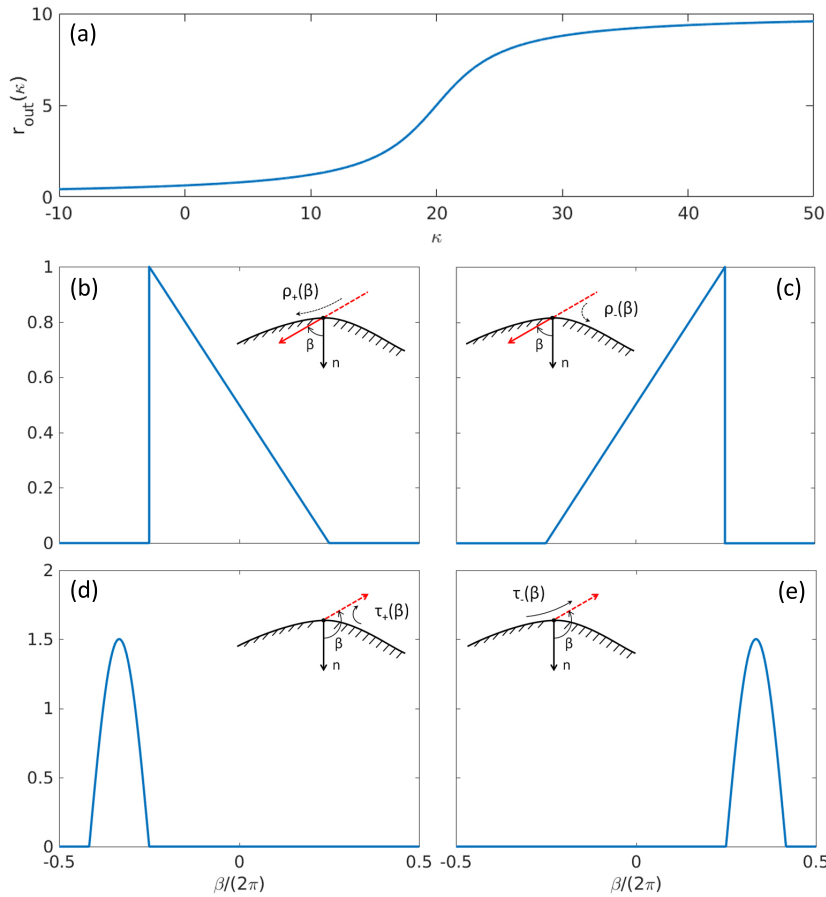
FIG. 5. *Functions $r_{\mathrm{out}}(\kappa)$, $\rho_\pm(\beta)$, and $\tau_\pm(\beta)$ used in the simulations. (a) The graph of $r_{\mathrm{out}}(\kappa) = \frac{10}{\pi}\arctan\left(\frac{\kappa - 20}{4}\right) + 5$. It is positive, increasing in κ, and bounded as $\kappa \to +\infty$. (b)–(e) The graphs of functions $\rho_\pm(\beta)$ and $\tau_\pm(\beta)$. The insets illustrate the situations where these functions come into play; see (3.2), (3.3), and Figure 4 for more details. $\tau_\pm$ are normalized in the sense that $\int_{-\pi}^{\pi} \tau_\pm(\beta)\, d\beta = 1$.*

4.1. The effect of post spacings. Our first numerical simulation is devoted to investigating how post spacings affect the normalized net flux $E(\Omega)$. To be more precise, we fix the shape of the post specified later, and change the size of the unit cell specified by a and b, to see how $E(\Omega)$ changes correspondingly. Note that the set Ω implicitly depends on both a and b.

The post used in this simulation has a teardrop-shaped cross-section, defined by two circular arcs smoothly connected by two straight lines; see Figure 2(b). Under the nondimensionalization, the radii of the larger and the smaller circular arcs are 0.192 and 0.0154, respectively. Their corresponding dimensionless curvatures κ are 5.21 at the large end and 65.1 at the small tip, respectively. The angle between the two straight sides is 48 degrees. The tip of the post points to the positive x_2-direction. The dimensionless size of the post is approximately 0.642 in the vertical direction and 0.384 in the horizontal direction. Its perimeter is approximately 1.59.

In Figure 6, we show how $E(\Omega)$ changes as we vary the dimensionless width a and
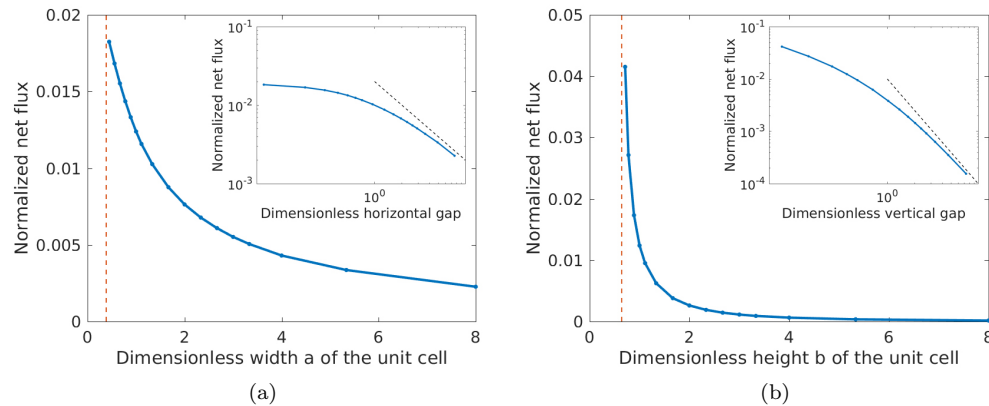
FIG. 6. *The normalized net flux $E(\Omega)$ depending on the dimensionless width a and the height b of the unit cell. (a) With $b = 1$, $E(\Omega)$ decreases as a increases. The red dashed line indicates the minimum possible width $a_{min} = 0.384$. The inset shows a log-log plot of $E(\Omega)$ depending on the dimensionless horizontal gap, $a - a_{min}$. The black dashed line in the inset has slope -1. (b) With $a = 1$, $E(\Omega)$ decreases as b increases. The red dashed line indicates the minimum possible height $b_{min} = 0.642$. The inset is a log-log plot of $E(\Omega)$ depending on the dimensionless vertical gap, $b - b_{min}$. The black dashed line in the inset has slope -2. (Color available online.)*

height b of the unit cell. These results are obtained by solving the model (2.7)–(2.11) for each pair of (a, b) and calculating the corresponding $E(\Omega)$. In Figure 6(a), we fix $b = 1$ and vary a. It shows that $E(\Omega)$ decreases as a increases. The red dashed line indicates the minimum a ($a_{min} = 0.384$) we can possibly achieve, in which case the neighboring teardrop-shaped posts will touch each other. As a approaches a_{min}, $E(\Omega)$ converges to a finite value. The inset of Figure 6(a) shows a log-log plot of $E(\Omega)$ versus $a - a_{min}$. The black dashed line in the inset has slope -1, which implies that when a is large, $E(\Omega)$ decays like $(a - a_{min})^{-1}$ or, equivalently, as a^{-1}. In Figure 6(b), we take $a = 1$ and vary b. $E(\Omega)$ decreases as b increases. The red dashed line again indicates the minimum b ($b_{min} = 0.642$) we can achieve, when the teardrop-shaped posts in two neighboring rows will touch each other. When b approaches b_{min}, $E(\Omega)$ apparently diverges to infinity. The inset of Figure 6(b) shows a log-log plot of $E(\Omega)$ versus $b - b_{min}$. The black dashed line in the inset has slope -2. In other words, when b is large, $E(\Omega)$ decays like $(b - b_{min})^{-2}$ or, equivalently, b^{-2}.

The above results agree with the intuition that the open-space swimming away from the boundary smears out the anisotropy or bias [40] in the swimming direction induced by the boundary shape, thus making $E(\Omega)$ weaker. As a result, $E(\Omega)$ should get boosted if we compress the open space by shrinking the gaps between neighboring posts in both directions. Indeed, shrinking b might be particularly effective due to the unboundedness of the graph in Figure 6(b) when $b \to b_{min}$. However, we should remark that making the gaps too narrow is not always favored in practice. Swimming rods can run into each other or even cause traffic jams in very narrow gaps, which impairs their mobility and makes the directed migration weaker. Narrow gaps may significantly change the swimming behavior of the self-propelled rods, which is not considered in our model. For example, experiments show that active rods can increase speed by up to five times in confining channels with a ceiling [19]. Further, the size of the rods, which is ignored in our model, becomes important when they swim in confined spaces like narrow gaps.

With this in mind, we study the net flux under a different normalization by normalizing the number of rods per unit area instead of one unit cell. This is more useful in practice, since we may use suspensions of swimming rods with some particular concentration to do experiments, and so the number of rods in the unit area is approximately given. In addition, we may want to compute the net flux per unit width of array, since that characterizes the efficacy of the whole device in transporting rods within horizontal cross-sections of unit length. The net flux under this new normalization is thus given by $\tilde{E}(\Omega) = abE(\Omega)/a = bE(\Omega)$, which is the net flux over unit horizontal cross-section with the rod concentration normalized.

From the discussion above, it is known that when a or b is large, $\tilde{E}(\Omega)$ should decay like a^{-1} or b^{-1}, respectively. This can be justified by the following formal analysis.

1. When b is fixed and a is large, posts in different vertical columns function almost independently as they are so far away. That a gets doubled is almost equivalent to removing half of the posts in one row, which will naturally decrease $\tilde{E}(\Omega)$ by one-half. This implies that $\tilde{E}(\Omega)$ will decay like a^{-1} when a is large.

2. When a is fixed and b is large, posts in different rows are now far away from each other. If a rod leaves a post and swims into the open space towards posts in another neighboring row, then midway its orientation is already randomized. An important length scale here is $v_0/D_r = 1$, which is the characteristic distance a rod can travel away from the post before it forgets its initial direction when leaving the boundary. Therefore, $p(x, \theta)$ should have little θ-dependence when the distance between x and any posts in the array is significantly larger than 1. As a result, when b is large, the motion of the rods midway between two rows can be characterized by an enhanced isotropic diffusion with the effective diffusion coefficient $D_{\text{eff}} = D_t + \frac{v_0^2}{4D_r}$ [13]. Instead of (2.7), one can solve $D_{\text{eff}}\Delta\tilde{p}(x) = 0$ for the spatial distribution of rods, while the orientational distribution of rods there should be almost uniform in all directions. From the far-field point of view, the effect of one post can be modeled as a dipole in the positive x_2-direction, since it effectively sucks rods from one end (the larger end) and releases them from the other (the smaller tip). The dipole magnitude is insensitive to b, since we have normalized the rod concentration instead of the number of rods per unit cell. Hence, the far-field spatial density of rods $\tilde{p}(x)$ induced by one single dipole at the origin, up to an additive constant, can be approximated by $\tilde{p}(x) \sim \frac{Cx_2}{x_1^2+x_2^2}$. Here C is a constant depending on D_{eff} and the dipole magnitude.

   We align such a dipole in an array with horizontal spacing a and vertical spacing b and calculate the net flux crossing the segment $\{(x_1, x_2) : x_1 \in [-a/2, a/2], x_2 = b/2\}$. We start from one row of posts all centered at $x_2 = 0$. The spatial density in a neighborhood of the line $x_2 = b/2$ contributed by this row should be well approximated, up to an additive constant, by $\tilde{p}_0(x) = \sum_{k \in \mathbb{Z}} \tilde{p}(x_1 + ka, x_2)$. By (2.13), the net flux contributed by this row is given by

$$\tilde{E}_0 = \int_{\partial\Omega \cap \{x_2=b/2\}} -D_t\frac{\partial\tilde{p}_0}{\partial x_2} + v_0\tilde{p}_0 \sin 2\pi\theta \, dA.$$

The subscripts 0 imply that this portion of the net flux comes from the row of posts centered at $x_2 = 0$ (i.e., $\tilde{p}_0$). The second term in the integral above

should vanish, since $\tilde{p}_0(x)$ does not depend on θ. Hence,

$$
\tilde{E}_0 = -D_t \left[\int_{-a/2}^{a/2} \frac{\partial \tilde{p}_0}{\partial x_2} \, dx_1 \right]_{x_2=b/2} = -D_t \left[\int_{\mathbb{R}} \frac{\partial \tilde{p}}{\partial x_2} \, dx_1 \right]_{x_2=b/2}
$$

$$
= -D_t \left[\int_{\mathbb{R}} \partial_{x_2} \left(\frac{Cx_2}{x_1^2 + x_2^2} \right) dx_1 \right]_{x_2=b/2} = \frac{C_0}{b},
$$

where C_0 is a positive constant depending on D_t, D_{eff}, and the dipole magnitude. By symmetry, the net flux contributed by the row of posts centered at $x_2 = b$ should be $\tilde{E}_1 = \tilde{E}_0$. For the rows of posts farther away from the line $x_2 = b/2$, their contributions to the net flux are suppressed by the screening effect of the rows that are closer to $x_2 = b/2$. Indeed, the probability of a rod leaving a post centered at $x_2 = kb$ and reaching the horizontal line $x_2 = b/2$ without being captured by any other posts on the way should decay exponentially as $|k - 1/2| \to \infty$; in other words, the contributions to the net flux from these farther rows cannot be fully seen by the line $x_2 = b/2$ due to the existence of closer rows. Assume the screening factor to be α_k for the row of posts centered at $x_2 = kb$, with $\sum_{k \in \mathbb{Z}} \alpha_k < \infty$. We write the contribution of the row centered at $x_2 = kb$ to the net flux crossing the segment $\{(x_1, x_2) : \ x_1 \in [-a/2, a/2], \ x_2 = b/2\}$ to be $\tilde{E}_k = \alpha_k \tilde{E}_0$. Presumably, α_k's should be independent of b, but only depend on the horizontal spacing of neighboring posts in one row, which is fixed here. The total net flux induced by the whole array then becomes $\tilde{E}(\Omega) = \sum_{k \in \mathbb{Z}} \alpha_k \tilde{E}_0 = \frac{\tilde{C}}{b}$, where $\tilde{C}$ is a constant depending on α_k's, D_t, D_{eff}, and the dipole magnitude, but independent of b. This justifies the b^{-1}-decay of $\tilde{E}(\Omega)$ when b is large.

4.2. Optimization of post shape. In the second family of simulations, we fix the size of the unit cell by setting $a = b = 1$, and we apply the shape optimization method mentioned in subsection 2.2 to find posts that induce larger normalized net flux $E(\Omega)$. See sections SM3–SM5 of the supplementary material for the complete mathematical derivations of the equations involved, and see section SM6 for the numerical methods. The parameters and rates have been chosen in section 3.

We start with the post in the convex teardrop shape introduced in subsection 4.1. Figure 7(a) shows the comparison before and after we apply the shape optimization to the teardrop-shaped candidate. The blue curve represents the initial shape, while the red curve is the optimized one (the final shape). Note that the iterative optimization gets terminated when the post gets too close (dimensionless distance ≤ 0.02) to the border of the unit cell. We observe that with shape optimization, the post swells significantly and becomes nonconvex; the former agrees with the earlier observation that, in general, smaller gaps between neighboring posts imply larger flux. A small round head forms at the top, connected by a thin neck to the larger belly. The dimensionless curvature around the head is in a narrow range $[24.5, 25.5]$; recall that it is 65.1 at the tip of the initial shape. The side parts of the post, initially flat, become slightly wavy. This can be artificial since only low-frequency modes are used in describing the boundary evolution. Indeed, we use 240 equally spaced points to represent the curve, but only the first 41 Fourier modes are used in the boundary evolution. See section SM6 of the supplementary material for more details about the numerical method. The lower half of the post largely remains a circular arc. In the course of the shape optimization, $E(\Omega)$ increases almost sevenfold, from 1.24×10^{-2} to 8.44×10^{-2}.
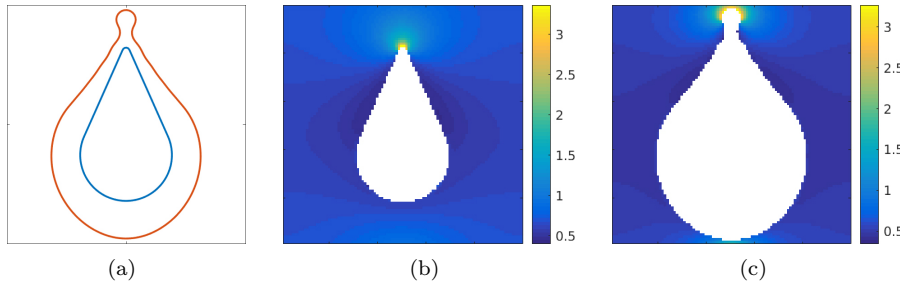
FIG. 7. *Performing shape optimization of a teardrop-shaped post.* (a) *The initial and the optimized shapes are represented by blue and red curves, respectively. In the course of the shape optimization, the post swells, with the sharp tip at the top evolving into a small round head. The lower half of the post remains a circular arc, while the overall post shape becomes nonconvex.* $E(\Omega)$ *increases from* 1.24×10^{-2} *to* 8.44×10^{-2}. (b)–(c) *The spatial concentrations of rods* $c(x)$ *in the presence of the posts with the initial and the optimized shapes in* (a) *are plotted in* (b) *and* (c), *respectively. The fraction of rods captured on the post boundary is not included in these figures.* (Color available online.)

To investigate how rods are spatially distributed in the presence of posts with the initial and optimized shapes shown in Figure 7(a), we plot in Figures 7(b) and 7(c) their corresponding spatial concentrations of rods $c(x) \triangleq \int_0^1 p(x, \theta) \, d\theta$ for $x \in \omega$. Note that the fraction of rods captured on the boundary is not included. Figures 7(b) and 7(c) share some common features:

1. The rod concentrations in both cases have their peaks near the top of the posts, implying that the top parts are the sites where strong net desorption occurs.
2. There are regions of strong depletion near the flat sides of the posts.
3. The rod concentrations around the bottoms are also relatively high, due to the high concentrations near the tops of the posts in the next unit cells directly below.
4. The rod concentrations in both cases have a negative normal derivative near the bottom of the posts (i.e., $c(x)$ decreases when we approach the bottom from some distance away), which implies that the bottoms are effectively absorbing rods.

These features are also seen in our earlier experiments [40, inset of Fig. 3]; in fact, Figure 7(b) agrees particularly well with the experimental results, except that here we do not plot the "boundary layer" of rods trapped along the post boundary. This suggests that our model effectively describes the real situation.

The main difference between Figure 7(b) and 7(c) is that the area of the strong desorption site at the top in Figure 7(c) is much larger than that in Figure 7(b), although the curvature there ($\kappa \in [24.5, 25.5]$) is much smaller than that ($\kappa = 65.1$) in the initial shape. This can partially explain why the optimized shape can induce a much larger net flux.

Next, we apply the shape optimization to a new nut-shaped post. The motivation of choosing this as the new initial shape is that the head-forming process can potentially increase $E(\Omega)$. It might accelerate this process if we start from an initial shape which already has a head. In Figure 8(a), we plot the shape of post before and after the shape optimization. Again, the blue curve represents the initial shape, while the red curve is the final one. The normalized net flux increases from 1.81×10^{-2} to
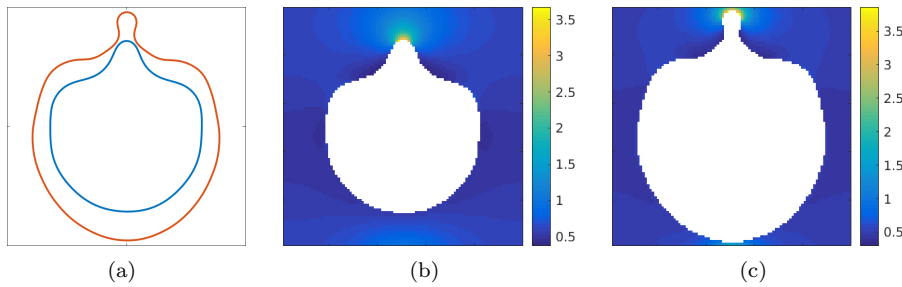
FIG. 8. *Performing shape optimization of a nut-shaped post.* (a) *The initial and the optimized shapes are represented by blue and red curves, respectively. In the course of the shape optimization, the post swells and a small round head forms at the top, while the lower half of the post remains a circular arc.* $E(\Omega)$ *increases from* 1.81×10^{-2} *to* 7.82×10^{-2}*.* (b)–(c) *The spatial concentrations of rods* $c(x)$ *in the presence of the posts with the initial and the optimized shapes in* (a) *are plotted in* (b) *and* (c)*, respectively. Again, the fraction of rods captured on the post boundary is not included. (Color available online.)*

7.82×10^{-2}, which is a big improvement but not as good as the previous case. We see that once again the shape swells to fill almost the whole height of the unit cell; a round head and a neck forms at the top, while the lower half of the post largely remains a circular arc. The dimensionless curvature at the head of the final shape ranges in $[24, 25.5]$. Again we plot the spatial concentrations of rods corresponding to posts with the initial and optimized shapes in Figures 8(b) and 8(c), respectively. It is clear that the top parts of both posts are the strong desorption sites, while it is larger in the optimized shape than in the initial shape. In addition, there are noticeably two more sites near the post boundary with relatively high rod concentration and positive normal derivatives of $c(x)$. They are the "shoulders" of both the initial and the optimized shapes, which refer to the curved parts on both sides of the posts; they are also efficient in releasing rods. The bottoms of the posts are the main absorption sites as before.

The effect of the "shoulders" on the net flux is unclear though. The net flux can benefit from larger desorbing sites. On the other hand, however, the shoulders are not as efficient desorbing sites as the heads at the top, since the shoulders are far away from the top border of the unit cell and the rods released there may fail to reach the top border. In this sense, the presence of the shoulders can impair the capability of the head releasing rods at the top, and thus reduce $E(\Omega)$. This may explain why the optimized shape in this case does not have as high $E(\Omega)$ as the one in Figure 7(a).

It is shown in subsection 4.1 that shrinking gaps between neighboring posts, especially the vertical gap, can effectively increase $E(\Omega)$. One may question whether the increase in $E(\Omega)$ in the two cases above is purely due to the enlargement of the post (and thus shrinking of the vertical gap), or whether it does benefit from the changes in shape. To rule out the first possibility, we make up enlarged copies of the initial teardrop-shaped and nut-shaped posts, such that they have the same height (and thus the same vertical gaps between neighboring posts) as their corresponding optimized shapes. We plot the boundaries of enlarged posts in Figure 9 using solid curves, together with the corresponding optimized shapes that are plotted as dashed curves. We calculate $E(\Omega)$ for the enlarged posts. The enlarged teardrop-shaped post induces a normalized net flux 5.00×10^{-2}, and the enlarged nut-shaped post gives 2.58×10^{-2}. In both cases, the enlarged posts can generate much larger net fluxes
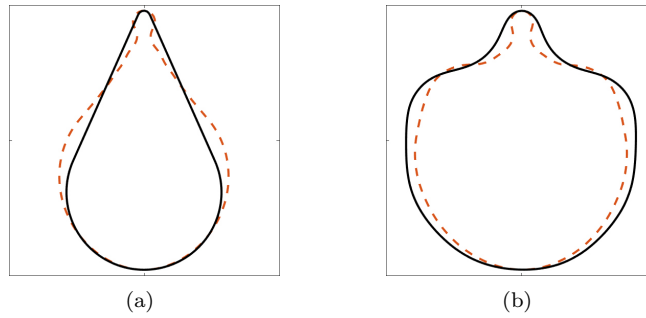
FIG. 9. *Enlarged posts with the initial shapes (solid curves) and posts with the optimized shapes (dashed curves). The heights of the enlarged posts are set to be the same as their corresponding optimized posts.*
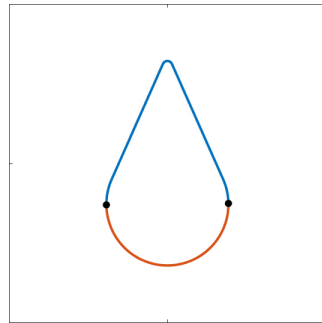

FIG. 10. *Dividing the post boundary γ into its upper (blue) and lower (red) halves in the case of a teardrop-shaped post. The left- and rightmost points on γ are marked as black dots. (Color available online.)*

than the original ones, but still cannot compete with the optimized shapes. In this way, we justify that the shape optimization does help us find better post designs.

To summarize, in addition to the overall swelling of the post in the shape optimization, we empirically find different evolutions of the upper and lower halves of the post boundary. Round heads tend to form at the top of the posts, with curvature there being in a narrow range $\kappa \in [24.5, 26]$; a convex shape can evolve to become nonconvex. By contrast, the lower half of the post always prefers to be a circular arc.

5. An approximate, but informative, analysis. To better understand our findings and explore the possibility of designing posts with yet better shapes, we consider a simplified model. We divide the post boundary curve γ into its upper and lower halves by cutting it at the leftmost and the rightmost points on γ. If there are several such points, pick the lowest one whenever necessary. See Figure 10 for an illustration. We denote the upper and lower halves of γ by γ_U and γ_L, respectively. Since $r_{\mathrm{in}} \equiv 1$ on γ, when there is no a priori information about the spatial distribution of rods, then

$$F_U \triangleq \int_{\gamma_U} r_{\mathrm{out}}(\kappa(s)) \, ds$$

becomes a good characterization of the capability of γ_U releasing rods. Here s is the

arclength parameter of γ. Similarly,

$$F_L \triangleq \int_{\gamma_L} r_{\mathrm{out}}(\kappa(s)) \, ds$$

is the corresponding quantity for γ_L. We naively assume that rods leaving from γ_U are more likely to reach the top border of the unit cell than the bottom border, while rods released from γ_L are more likely to cross the bottom border. By this assumption, rods of the former type contribute positively to $E(\Omega)$ since they cross the border in the positive x_2-direction, while those of the latter type contribute negatively. Hence, in a simplified manner, we use $F_U - F_L$ to characterize the overall capability of γ inducing spontaneous migration in the positive x_2-direction. Here we ignore the variance in position and orientation of rods when they cross either part of the boundary, and neither do we incorporate any information about the spatial distribution of rods. Therefore, to find a post with a good shape, we formally consider the following optimization problem:

$$(5.1) \qquad \max_{\gamma}(F_U - F_L) = \max_{\gamma}\left[\int_{\gamma_U} r_{\mathrm{out}}(\kappa(s)) \, ds - \int_{\gamma_L} r_{\mathrm{out}}(\kappa(s)) \, ds\right].$$

Here $r_{\mathrm{out}}(\kappa)$ is given by (3.1), and we take maximum over all admissible curves γ. By admissible, we mean γ that is sufficiently smooth and that does not intersect with itself. If needed, we may also impose a constraint that the curvature of γ is bounded above and below by some constants.

To formally solve the maximization problem (5.1), we first note that

$$(5.2) \qquad \max_{\gamma}(F_U - F_L) \leq \max_{\gamma} \int_{\gamma_U} r_{\mathrm{out}}(\kappa(s)) \, ds - \min_{\gamma'} \int_{\gamma'_L} r_{\mathrm{out}}(\kappa(s)) \, ds.$$

On the right-hand side, the γ that attains the maximum in the first term and the γ' that attains the minimum in the second term do not have to be the same one. The famous Gauss–Bonnet theorem [8] will be useful in the following discussion, which states that for any admissible γ in our context,

$$(5.3) \qquad \int_{\gamma_U} \kappa(s) \, ds = \int_{\gamma_L} \kappa(s) \, ds = \pi,$$

where s is the arclength parameterizing γ in a counterclockwise orientation.

We first consider the maximizing problem in (5.2). We rewrite

$$\max_{\gamma} \int_{\gamma_U} r_{\mathrm{out}}(\kappa(s)) \, ds = \max_{\gamma} \int_{\gamma_U} \frac{r_{\mathrm{out}}(\kappa(s))}{\kappa(s)} \kappa(s) \, ds.$$

Here $r_{\mathrm{out}}(\kappa)/\kappa$ can be understood as the efficiency of utilizing the curvature to generate a desorption flux, given that (5.3) implies a fixed "budget" of the curvature on both γ_U and γ_L. In order for the integral to be maximized, $r_{\mathrm{out}}(\kappa)/\kappa$ needs to be as large as possible when $\kappa > 0$ and as small as possible when $\kappa < 0$. It is known by (3.1) that $r_{\mathrm{out}}(\kappa)/\kappa \to \pm\infty$ as $\kappa \to 0^{\pm}$. Moreover, it is easy to show that $r_{\mathrm{out}}(\kappa)/\kappa$ reaches a local maximum at $\kappa_{\max} \approx 25$. See Figure 11. This implies that in the upper half of the post, the curvature tends to be close to 0 or $\kappa_{\max}$. This explains why the curvature at the heads in both examples above lies in a narrow range close to 25 instead of even larger values, such as $\kappa = 65.1$ at the tip of the initial teardrop-shaped post. In
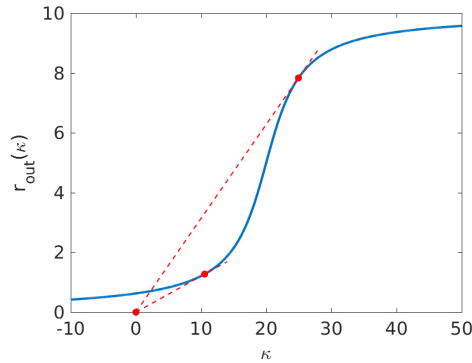
FIG. 11. $r_{\mathrm{out}}(\kappa)/\kappa$ reaches a local maximum at $\kappa_{\max} \approx 25$ and a local minimum at $\kappa_{\min} \approx 10.5$, marked as red dots on the curve. Note that $r_{\mathrm{out}}(\kappa)/\kappa$ is the slope of straight line connecting the point $(\kappa, r_{\mathrm{out}}(\kappa))$ with the origin. (Color available online.)

addition, it does no harm to have negative curvature in γ_U as it potentially increases the arclength where the $\kappa_{\max}$ could be attained, thus improving the overall capability of γ_U releasing rods. This explains why convex shapes can evolve into nonconvex ones in the shape optimization.

Now we turn to the minimization problem involving γ'_L in (5.2). We note that $r_{\mathrm{out}}(\kappa)/\kappa$ has a local minimum at $\kappa_{\min} \approx 10.5$. See Figure 11. If we rule out the case when κ can be very large along γ'_L, say assuming $\kappa < 80$, we will find

$$r_{\mathrm{out}}(\kappa) \geq \frac{r_{\mathrm{out}}(\kappa_{\min})}{\kappa_{\min}}\kappa \quad \forall\, \kappa < 80.$$

Hence,

$$\min_{\gamma'} \int_{\gamma'_L} r_{\mathrm{out}}(\kappa(s))\, ds \geq \frac{r_{\mathrm{out}}(\kappa_{\min})}{\kappa_{\min}} \int_{\gamma'_L} \kappa(s)\, ds = \frac{\pi r_{\mathrm{out}}(\kappa_{\min})}{\kappa_{\min}}.$$

Therefore, the minimum is achieved if γ'_L is a semicircle with dimensionless curvature $\kappa_{\min}$. This might not be obtained in general, because, for example, the arclength between the leftmost and the rightmost points on γ' may not match the arclength of the semicircle with curvature $\kappa_{\min}$. In such a case, γ'_L still has to be largely a semicircle. We can prove this under the assumption that $\kappa < 20$ on γ'_L simply by noticing that $r_{\mathrm{out}}(\kappa)$ is a convex function for $\kappa < 20$ and then applying Jensen's inequality.

6. Explorations of other designs. In what follows, we shall design better posts based on the above simulations and analysis. We have seen that the round heads formed in Figures 7(a) and 8(a) act as strong desorption sites, which contribute a lot to increase $E(\Omega)$. It is natural to believe that $E(\Omega)$ can benefit from putting more strong desorption sites close to the top border of the unit cell. This inspires us to consider the new posts plotted in Figures 12(a) and 12(c), with multiple fingers at the top. Indeed, we choose these two shapes, such that the curvature at all fingertips satisfies $\kappa \in [23, 26]$, presumably making them into strong desorption sites. In addition, we take the lower halves of these two shapes to be largely circular arcs. We compute $E(\Omega)$ for these two posts, without performing shape optimization. For the three-finger post, $E(\Omega) = 4.78 \times 10^{-2}$; for the five-finger post, $E(\Omega) = 6.18 \times 10^{-2}$, already close to our optimized single-head case. The spatial concentrations of the rods corresponding to these two
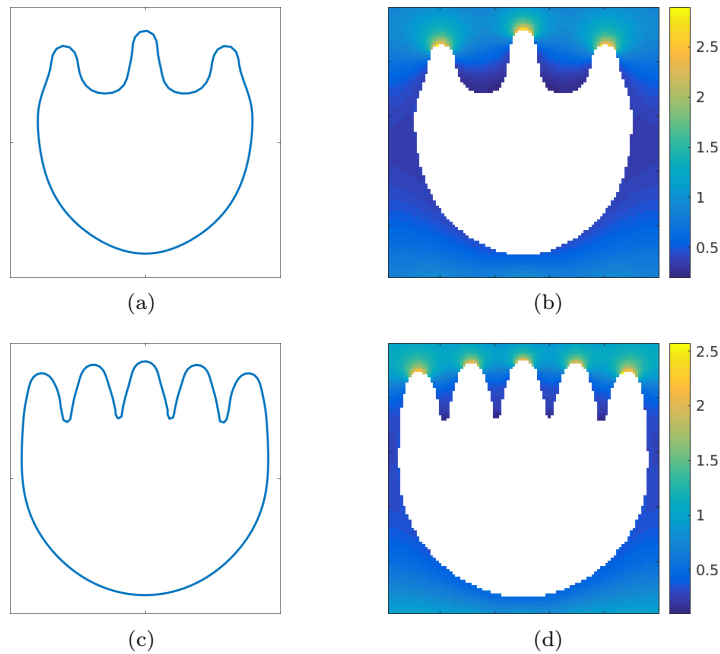
(a)   (b)

(c)   (d)

FIG. 12. *Two new candidate post shapes with multiple fingers at the top as strong desorption sites. All fingertips have curvature $\kappa \in [23, 26]$ at the top, while the lower halves of the posts are designed to be largely circular arcs. (a)–(b) The three-finger post and its induced spatial rod concentration. In this case, $E(\Omega) = 4.78 \times 10^{-2}$. (c)–(d) The five-finger post and its induced spatial rod concentration. In this case, $E(\Omega) = 6.18 \times 10^{-2}$.*

candidate posts are also plotted in Figure 12(b) and Figure 12(d), respectively. It is clear that all the finger tips in both shapes are indeed strong desorption sites that are close to the top border of the unit cell. Efforts are being made to experimentally study the directed migration of swimmers induced by such posts with complex shapes.

Although these multifinger posts already give strong net flux even without shape optimization, they still cannot compete the final optimized shape we obtained in Figure 7(a). One of the reasons is that there are still lots of open spaces between the post and the border of the unit cell. In particular, further reducing the vertical gap by enlarging the posts can hopefully lead to stronger fluxes. Another reason is the suboptimality of their shapes. For example, the curvatures of the lower half of these two posts are not close to $\kappa_{\min}$ found before. We also note that if we change the fingertips into small round heads with curvature close to $\kappa_{\max}$, the area of the strong desorption site can increase considerably, and thus $E(\Omega)$ may increase as well.

Now we propose a shape that is almost the optimal in the sense that it leaves very little open space for the free swimming of the rods, and it almost solves the simplified optimization problem on the right-hand side of (5.2) by putting the right curvatures in the upper and lower halves of γ. We plot it in Figure 13 using solid curves in a 2×5 array. The dashed box represents one unit cell of the array, with $a = 0.2$ and $b = 1$. The post within the box has a slim shape, whose height and width are 0.940 and 0.180, respectively. It has flat sides and curved top and bottom parts. The top part consists of two semicircular arcs with $\kappa \approx 23$, which is close to $\kappa_{\max} \approx 25$; the bottom part is a semicircular arc, with $\kappa \approx 11$, which is close to $\kappa_{\min} \approx 10.5$. There are
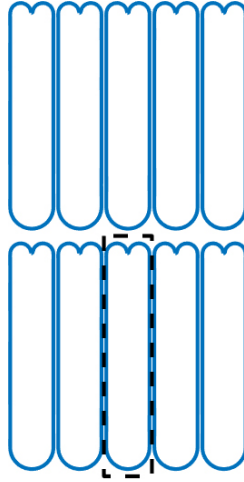
Fig. 13. *A 2×5 array of a slim post. Its unit cell has $a = 0.2$ and $b = 1$. The post has flat sides and curved top and bottom parts. The top part consists of two semicircles with $\kappa \approx 23$, while the bottom part is a semicircle with $\kappa \approx 11$. There are only narrow gaps between neighboring posts in the same row. Such an array induces a normalized net flux $E(\Omega) = 1.15 \times 10^{-1}$.*

only narrow gaps between neighboring posts. We compute its normalized net flux to obtain $E(\Omega) = 1.15 \times 10^{-1}$, which surpasses any other posts considered in this paper! Note that we do not rule out the existence of even more judicious designs of posts. In sum, we showed that using what we have learned in the numerical shape optimization and the formal analysis above, we can design better post shapes effectively.

7. Conclusion and discussion. In this paper, we propose a kinetic-type model to study Au-Pt rods swimming and directionally migrating in a periodic array of posts with noncircular cross-sections. Both position and orientation of the rods are taken into account. The absorption and desorption of the swimming rods on the post boundaries are modeled via empirically defined angular distributions and rate functions of the boundary curvature. Within this model, we define and compute the normalized net flux induced by a periodic rectangular array of posts, which characterizes the intensity of the spontaneous directed migration of rods in the array due to the asymmetry in geometry. We study how to design the array judiciously so that it can induce stronger directed migration. It is shown that the net flux increases if the horizontal and vertical spacings between neighboring posts shrink. On the other hand, we apply the numerical shape optimization to find better shapes of posts that induce yet larger flux. Inspired by the numerical results on two candidate posts—a teardrop-shaped post and a nut-shaped post, we propose a simplified model to show the key geometric features a good post should have. Based on that, we come up with three new candidate shapes that generate large fluxes. In this way, we show that the shape optimization technique can help design good posts effectively.

Our results crucially rely on the choices of (hopefully reasonable) universal rate functions $r_{\mathrm{in}}(\kappa)$ and $r_{\mathrm{out}}(\kappa)$, and the angular distributions $\rho_{\pm}(\beta)$ and $\tau_{\pm}(\beta)$, for which little experimental measurement exists. In this paper, we choose these functions so that they qualitatively agree with the existing experimental observations and physical intuition. We note that our choices of $\rho_{\pm}(\beta)$ and $\tau_{\pm}(\beta)$ are natural and reasonable. The numerical experience is that, even if we alter the choice of these angular distri-

butions, the numerical results are qualitatively unchanged. By contrast, $r_{\mathrm{in}}(\kappa)$ and $r_{\mathrm{out}}(\kappa)$ could have bigger impacts on the numerical results. It has been shown in the simplified model in section 4 that, given $r_{\mathrm{in}} \equiv 1$, the local maximum and minimum of $r_{\mathrm{out}}(\kappa)/\kappa$ can be very crucial quantities that determine geometric features of a good post. For example, if we alternatively take $r_{\mathrm{out}}(\kappa)$ to be e^{κ}, one would expect a good post to have very sharp tips at its top instead of small round heads or circular arcs, since $r_{\mathrm{out}}(\kappa)/\kappa$ formally achieves maximum at $\kappa = +\infty$. If we further choose $r_{\mathrm{in}}(\kappa)$ to be a function depending on κ, the situation would be more complicated and it can hardly be characterized by our simplified model.

In the current model, the absorption and desorption of the swimming rods on the post boundary are handled in a phenomenological manner, which is the reason we need the functions above. It would be ideal to build up a hydrodynamic model to fully characterize the interaction between the swimming bimetallic rods and the curved solid boundary, from which we can hopefully derive the rate functions and angular distributions that are needed. Previous work by Takagi et al. [33] applying lubrication theory between a swimming rod and a flat solid boundary cannot be immediately generalized to the case of the curved boundary, especially when the radius of curvature of the boundary is on the same scale as or even below that of the rod length, which is the case when a rod comes to the sharp tip of a teardrop-shaped post. Spagnolie et al. [31] model the hydrodynamic capture and escape of microswimmers on an obstacle by assuming the swimmers are force dipoles. However, this analysis assumes that the swimmer can preserve its orientation when it hits the boundary, which is not true in our case. More delicate modeling is thus needed to understand the hydrodynamic interaction between swimmers and complex boundaries in fluid environments.

REFERENCES

[1] J. L. ANDERSON, *Colloid transport by interfacial forces*, Annu. Rev. Fluid Mech., 21 (1989), pp. 61–99, https://doi.org/10.1146/annurev.fl.21.010189.000425.

[2] S. BALASUBRAMANIAN, D. KAGAN, C.-M. J. HU, S. CAMPUZANO, M. J. LOBO-CASTAÑON, N. LIM, D. Y. KANG, M. ZIMMERMAN, L. ZHANG, AND J. WANG, *Micromachine-enabled capture and isolation of cancer cells in complex media*, Angewandte Chemie Internat. Ed., 50 (2011), pp. 4161–4164, https://doi.org/10.1002/anie.201100115.

[3] H. C. BERG, D. A. BROWN, ET AL., *Chemotaxis in Escherichia coli analysed by three-dimensional tracking*, Nature, 239 (1972), pp. 500–504, https://doi.org/10.1038/239500a0.

[4] A. P. BERKE, L. TURNER, H. C. BERG, AND E. LAUGA, *Hydrodynamic attraction of swimming microorganisms by surfaces*, Phys. Rev. Lett., 101 (2008), 038102, https://doi.org/10.1103/PhysRevLett.101.038102.

[5] L. CISNEROS, C. DOMBROWSKI, R. E. GOLDSTEIN, AND J. O. KESSLER, *Reversal of bacterial locomotion at an obstacle*, Phys. Rev. E, 73 (2006), 030901, https://doi.org/10.1103/PhysRevE.73.030901.

[6] M. CONTINO, E. LUSHI, I. TUVAL, V. KANTSLER, AND M. POLIN, *Microalgae scatter off solid surfaces by hydrodynamic and contact forces*, Phys. Rev. Lett., 115 (2015), 258102, https://doi.org/10.1103/PhysRevLett.115.258102.

[7] M. C. DELFOUR AND J.-P. ZOLÉSIO, *Shapes and Geometries: Metrics, Analysis, Differential Calculus, and Optimization*, 2nd ed., Adv. Des. Control 22, SIAM, Philadelphia, 2011,

https://doi.org/10.1137/1.9780898719826.

[8] M. P. Do Carmo, *Differential Geometry of Curves and Surfaces*, Vol. 2, Prentice-Hall, Englewood Cliffs, 1976.

[9] S. J. Ebbens and J. R. Howse, *In pursuit of propulsion at the nanoscale*, Soft Matter, 6 (2010), pp. 726–738, https://doi.org/10.1039/B918598D.

[10] J. Elgeti, R. G. Winkler, and G. Gompper, *Physics of microswimmers: Single particle motion and collective behavior: A review*, Rep. Progr. Phys., 78 (2015), 056601, https://doi.org/10.1088/0034-4885/78/5/056601.

[11] P. Galajda, J. Keymer, P. Chaikin, and R. Austin, *A wall of funnels concentrates swimming bacteria*, J. Bacteriology, 189 (2007), pp. 8704–8707, https://doi.org/10.1128/JB.01033-07.

[12] A. Ghosh and P. Fischer, *Controlled propulsion of artificial magnetic nanostructured propellers*, Nano Lett., 9 (2009), pp. 2243–2245, https://doi.org/10.1021/nl900186w.

[13] J. R. Howse, R. A. Jones, A. J. Ryan, T. Gough, R. Vafabakhsh, and R. Golestanian, *Self-motile colloidal particles: From directed propulsion to random walk*, Phys. Rev. Lett., 99 (2007), 048102, https://doi.org/10.1103/PhysRevLett.99.048102.

[14] V. Kantsler, J. Dunkel, M. Polin, and R. E. Goldstein, *Ciliary contact interactions dominate surface scattering of swimming eukaryotes*, Proc. Natl. Acad. Sci. USA, 110 (2013), pp. 1187–1192, https://doi.org/10.1073/pnas.1210548110.

[15] E. E. Keaveny, S. W. Walker, and M. J. Shelley, *Optimization of chiral structures for microscale propulsion*, Nano Lett., 13 (2013), pp. 531–537, https://doi.org/10.1021/nl3040477.

[16] G. Lambert, D. Liao, and R. H. Austin, *Collective escape of chemotactic swimmers through microscopic ratchets*, Phys. Rev. Lett., 104 (2010), 168102, https://doi.org/10.1103/PhysRevLett.104.168102.

[17] G. Li, J. Bensson, L. Nisimova, D. Munger, P. Mahautmr, J. X. Tang, M. R. Maxey, and Y. V. Brun, *Accumulation of swimming bacteria near a solid surface*, Phys. Rev. E, 84 (2011), 041932, https://doi.org/10.1103/PhysRevE.84.041932.

[18] G. Li and J. X. Tang, *Accumulation of microswimmers near a surface mediated by collision and rotational Brownian motion*, Phys. Rev. Lett., 103 (2009), 078101, https://doi.org/10.1103/PhysRevLett.103.078101.

[19] C. Liu, C. Zhou, W. Wang, and H. P. Zhang, *Bimetallic microswimmers speed up in confining channels*, Phys. Rev. Lett., 117 (2016), 198001, https://doi.org/10.1103/PhysRevLett.117.198001.

[20] E. Lushi, V. Kantsler, and R. E. Goldstein, *Scattering of biflagellate microswimmers from surfaces*, Phys. Rev. E, 96 (2017), 023102, https://doi.org/10.1103/PhysRevE.96.023102.

[21] J. G. Mitchell and K. Kogure, *Bacterial motility: Links to the environment and a driving force for microbial physics*, FEMS Microbiol. Ecol., 55 (2006), pp. 3–16, https://doi.org/10.1111/j.1574-6941.2005.00003.x.

[22] B. Mohammadi and O. Pironneau, *Applied Shape Optimization for Fluids*, Oxford University Press, New York, 2010, https://doi.org/10.1093/acprof:oso/9780199546909.001.0001.

[23] J. L. Moran and J. D. Posner, *Electrokinetic locomotion due to reaction-induced charge auto-electrophoresis*, J. Fluid Mech., 680 (2011), pp. 31–66, https://doi.org/10.1017/jfm.2011.132.

[24] J. Palacci, C. Cottin-Bizonne, C. Ybert, and L. Bocquet, *Sedimentation and effective temperature of active colloidal suspensions*, Phys. Rev. Lett., 105 (2010), 088304, https://doi.org/10.1103/PhysRevLett.105.088304.

[25] D. Patra, S. Sengupta, W. Duan, H. Zhang, R. Pavlick, and A. Sen, *Intelligent, self-powered, drug delivery systems*, Nanoscale, 5 (2013), pp. 1273–1283, https://doi.org/10.1039/C2NR32600K.

[26] W. F. Paxton, K. C. Kistler, C. C. Olmeda, A. Sen, S. K. St. Angelo, Y. Cao, T. E. Mallouk, P. E. Lammert, and V. H. Crespi, *Catalytic nanomotors: Autonomous movement of striped nanorods*, J. Amer. Chem. Soc., 126 (2004), pp. 13424–13431, https://doi.org/10.1021/ja047697z.

[27] O. Pironneau, *Optimal Shape Design for Elliptic Systems*, Springer Science & Business Media, New York, 2012, https://doi.org/10.1007/978-3-642-87722-3.

[28] J. Simmchen, J. Katuri, W. E. Uspal, M. N. Popescu, M. Tasinkevych, and S. Sánchez, *Topographical pathways guide chemical microswimmers*, Nature Commun., 7 (2016), 10598, https://doi.org/10.1038/ncomms10598.

[29] J. Sokolowski and J.-P. Zolesio, *Introduction to Shape Optimization*, Springer, Berlin, Heidelberg, 1992, https://doi.org/10.1007/978-3-642-58106-9.

[30] L. Soler, V. Magdanz, V. M. Fomin, S. Sanchez, and O. G. Schmidt, *Self-propelled micromotors for cleaning polluted water*, ACS Nano, 7 (2013), pp. 9611–9620, https:

//doi.org/10.1021/nn405075d.

[31] S. E. Spagnolie, G. R. Moreno-Flores, D. Bartolo, and E. Lauga, *Geometric capture and escape of a microswimmer colliding with an obstacle*, Soft Matter, 11 (2015), pp. 3396–3411, https://doi.org/10.1039/C4SM02785J.

[32] S. Sundararajan, P. E. Lammert, A. W. Zudans, V. H. Crespi, and A. Sen, *Catalytic motors for transport of colloidal cargo*, Nano Lett., 8 (2008), pp. 1271–1276, https://doi.org/10.1021/nl072275j.

[33] D. Takagi, J. Palacci, A. B. Braunschweig, M. J. Shelley, and J. Zhang, *Hydrodynamic capture of microswimmers into sphere-bound orbits*, Soft Matter, 10 (2014), pp. 1784–1789, https://doi.org/10.1039/C3SM52815D.

[34] P. Tierno, R. Golestanian, I. Pagonabarraga, and F. Sagués, *Magnetically actuated colloidal microswimmers*, J. Phys. Chem. B, 112 (2008), pp. 16525–16528, https://doi.org/10.1021/jp808354n.

[35] W. Uspal, M. N. Popescu, S. Dietrich, and M. Tasinkevych, *Self-propulsion of a catalytically active particle near a planar wall: From reflection to sliding and hovering*, Soft Matter, 11 (2015), pp. 434–438, https://doi.org/10.1039/C4SM02317J.

[36] G. Volpe, I. Buttinoni, D. Vogt, H.-J. Kümmerer, and C. Bechinger, *Microswimmers in patterned environments*, Soft Matter, 7 (2011), pp. 8810–8815, https://doi.org/10.1039/C1SM05960B.

[37] S. W. Walker and M. J. Shelley, *Shape optimization of peristaltic pumping*, J. Comput. Phys., 229 (2010), pp. 1260–1291, https://doi.org/10.1016/j.jcp.2009.10.030.

[38] Y. Wang, R. M. Hernandez, D. J. Bartlett, J. M. Bingham, T. R. Kline, A. Sen, and T. E. Mallouk, *Bipolar electrochemical mechanism for the propulsion of catalytic nanomotors in hydrogen peroxide solutions*, Langmuir, 22 (2006), pp. 10451–10456, https://doi.org/10.1021/la0615950.

[39] J. Wilkening and A. Hosoi, *Shape optimization of a sheet swimming over a thin liquid layer*, J. Fluid Mech., 601 (2008), pp. 25–61, https://doi.org/10.1017/S0022112008000384.

[40] M. S. D. Wykes, X. Zhong, J. Tong, T. Adachi, Y. Liu, L. Ristroph, M. D. Ward, M. J. Shelley, and J. Zhang, *Guiding microscale swimmers using teardrop-shaped posts*, Soft Matter, 27 (2017), pp. 4681–4688, https://doi.org/10.1039/C7SM00203C.